CSCanada
Advances in Petroleum Exploration and Development
Vol. 14, No. 1, 2017, pp. 1-17
DOI:10.3968/9886

ISSN 1925-542X [Print]
ISSN 1925-5438 [Online]
www.cscanada.net
www.cscanada.org

Prediction of Optimum Length to Diameter Ratio for Two-Phase Fluid Flow Development in Vertical Pipes

Joao Chidamoio[a],*; Lateef Akanji[a]; Roozbeh Rafati[a]

[a]School of Engineering, College of Physical Science, University of Aberdeen, AB24 3UE, UK.
*Corresponding author.

Supported by University of Aberdeen Project.

Received 10 July 2017; accepted 8 September 2017
Published online 26 September 2017

Abstract

We investigate, via numerical simulation technique, the effect of length-to-diameter ratio on transient air-water two-phase flow in vertically upward cylindrical pipe geometry for parameterisation of the pilot scale laboratory multiphase flow rig. Variables such as axial velocity along the leading Taylor bubble, Taylor bubble length and Taylor bubble velocity are considered. A hydrodynamic entrance length required to establish a fully developed two phase flow was critically evaluated. Aperiodic behaviour on time and space dictates the complexity of continuous and unstable gas liquid flow. The porous injection configuration produced small bubble sizes compared to a single gas injection configuration even at higher gas injection rates.

Average axial velocity of the leading Taylor bubble of 0.411, 0.424 and 0.451 m/s were obtained for *L*/*D* ratios of 16.6, 83.3 and 166.7 respectively. The eccentricity of the axial velocity on the leading Taylor bubble stream and on its nose is perceived from *L*/*D* ratio of 166.7. We obtained a power law function for the radial component of the axial velocity profile in the liquid film ahead of the leading Taylor bubble as $\frac{U}{U_{\max}} = \left(1 - \frac{r}{R}\right)^{\frac{1}{n}}$, with exponent n=16 for L/D =16.7, n=8 for L/D=83.3 and n=6 for L/D =166.7. Despite the decrease in the exponent as L/D ratio increases, a fully parabolic profile of the axial velocity on the liquid phase ahead of the Taylor bubble is not achieved. This, suggests that further studies on higher L/D ratios should be conducted.

Key words: Computer aided design; Finite elements; Hydrodynamic entrance length; Taylor bubble;

Chidamoio, J., Akanji, L., & Rafati, R. (2017). Prediction of Optimum Length to Diameter Ratio for Two-Phase Fluid Flow Development in Vertical Pipes. *Advances in Petroleum Exploration and Development*, *14*(1), 1-17. Available from: http://www.cscanada.net/index.php/aped/article/view/9886
DOI: http://dx.doi.org/10.3968/9886

INTRODUCTION

In oil industry, complex multiphase mixtures consisting of oil, gas, water and possibly precipitated solids and or formation sand may flow through the tubing with different flow regimes observed. The complexity of multiphase flow relies on properties such densities and viscosities and is also influenced by a complex heat transfer that occurs as fluids flow through the piping system and the mass transfer that takes place among the hydrocarbon fluids at the deformable interface.[1-3]

In the fully developed flow region of a pipe, the velocity profile does not change downstream, and thus the wall shear stress remains constant, perfectly symmetrical and the radial component profile of the axial velocity is fully parabolic.[4]

It has been reported that in fully developed continuous slug flow, no interaction between consecutive Taylor bubbles occurs. The bubbles rise at the same translational velocity of the length of the liquid slugs between them remaining constant.[5]

Signatures of probability density functions (PDF) have been used to identify the two phase flow regimes transitions.[6] Single peak at low void fraction was considered a bubbly flow regime, two-peaks as slug flow, single peak at high void fraction (void fraction) as annular flow and between slug flow and annular flow there is churn flow.

Observation of the characteristic behavior of slug frequency along the center line on air-water vertical upward flow in pipes can be used to evaluate the hydrodynamic entrance length.[7] The point at which the slug frequency becomes constant along the pipe length is considered as the entrance length. Therefore, a 60*D* entrance length was obtained. Paradoxically, overestimation of slug frequency was obtained by comparison with the model proposed by Hernandez-Perez et al.[8] and underestimation with a model proposed by Zabaras.[9]

Application of time series of void fraction and PDF of void fraction to determine the hydrodynamic entrance length has been implemented by Abdulkadir et al.[10] for vertical upward flow of air-water in 0.067 m inner diameter pipe. A slug flow pattern was considered to be fully developed in length of 60*D* pipe diameter based on PDF of void fraction that showed traditional features of slug flow (one peak at lower void faction representing liquid slug and one peak at higher void fraction denoting a Taylor bubble) in between 4.0 and 5.5 m in length. The results from CFD simulation were compared with the experiments and satisfactory agreement were obtained. However, this result cannot be up-scaled to a different height.

According to Brenn,[11] in single phase flow, it is well established that an entrance length of 30 to 50 diameters is necessary to establish fully developed flow in the turbulent regime. The corresponding minimum length threshold for multiphase flow to be fully developed is less well established and it is quite possible that some of the reported experimental observations are for temporary or developing flow patterns, argued Brenn and Wang et al.[11- 12] Similar argument has been made by Araujo et al.[13] Mayor et al.[14] and Morgado et al.[15] respectively. For a fully developed gas-liquid two-phase upward slug flow, the translational propagating velocity is independent of the length of the Taylor bubble.[16-20]

Measurements of slug length and the trailing Taylor bubble in vertical upward slug flow using optical probes and high speed motion analyser have been conducted by XIA et al. [21] They were able to derive a correlation between the trailing bubble velocity and the length of liquid slug. Better agreement was found in position of 1, while some discrepancies were observed at locations close to the pipe inlet at ; and respectively.

The minimum length of a stable liquid slug is equal to the distance from the Taylor bubble bottom to the position where the axial velocity in near wall approaches constant, stated Wang et al.[22]

Another complexity in obtaining fully developed gas-liquid flow is the expansion of the gas phase caused by the pressure changes along the tubing as it rises from the bottom of the well, leading to increase in bubble volume thereby affecting its motion.[3, 6, 15, 23]

Several investigators[24] have attributed a certain range of pipe length requirement for the full development of continuous slug flow, whilst others[25] have studied the effect of pipe diameter on the flow regime transition from slug to annular flow. In the former, lengths of between 50*D* and 70*D* and 70*D* and 100*D* were suggested for turbulent and laminar scenarios respectively. In the latter, an inner pipe diameter of 19 mm was investigated and compared with data bank from 5 to 70 mm diameter pipes.

The following length to diameter ratio correlation for fully developed slug flow was proposed by Taitel et al. [26]

$$\frac{L}{D} = 40.6\left(\frac{U_m}{\sqrt{gD}} + 0.22\right). \quad (1)$$

Where,U_m denote the average mixture velocity, *D* is the pipe diameter and g is the gravity acceleration.

In their investigations, based on slugging frequency decay, Kaji et al.[6] concluded that the flow pattern as well as slug lengths vary with the axial position. Although they did not find the exact axial distance at which the flow is fully developed, a Taylor bubble/liquid slug length of 100*D* was observed. Further, a gradual decrease of slug frequency was observed even at the furthest measurement point of 151.2*D*.

The work of Sharaf et al.[27] demonstrated that the flow pattern transitions during gas-liquid flow are not sharp rather a gradual shift from the characteristic of one flow pattern to those of another. Wisps of different sizes have been observed over most of the flow rates studied in gas-liquid two phase co-current flow in a vertical riser of 12.7 cm inner diameter.

The fully developed slug flow was characterised by Rosa and Souza [28] as the one where the liquid and gas velocity profiles no longer change within the liquid slug, the neighboring Taylor bubbles do not merge and the bubbles coalescence rate is null.

It is generally expected that, very long tubes are required to achieve fully developed continuous slug flow. This is as a result of the occurrence of bubble coalescence in the hydrodynamic entrance region where the alteration of the flow pattern along the tubing usually manifests.[14-15, 28-29]

From the above reported investigations, it can be concluded that, whilst a lot has been done in understanding the effect of pipe length, diameter and axial location on flow transition and regime development, there is yet to be an established relationship between the length-to-diameter ratio and the evolution/devolution sequence of the full parabolic profile observable in gas-liquid flow.

In this work, we investigate via numerical simulation technique, the effect of length-to-diameter ratio on transient air-water two-phase flow in vertically upward cylindrical pipe geometry for parameterisation of the pilot scale laboratory multiphase flow rig.

1. METHODOLOGY

A numerical model is formulated to establish the variations of phenomenological behaviour in the parameters associated with two phase flow developments by running a sensitivity analysis of variables such as the length to diameter ratio. The models dimensions are presented in Table 1.

First, several cylindrical pipe geometries of varying lengths were constructed using Computer-Aided-Design (CAD) package tool. The CAD tool allows for Non-Uniform Rational B-spline (NURBS) curves and surfaces of order 3 to be used in order to accurately capture the curvatures with tolerance-based level of detail, at the injections points along the pipe length.[30] Absolute tolerance of 10^{-9} meters; relative tolerance of 10^{-7}% and angle tolerance of 10^{-3} degree, were applied in order to differentiate all the discernible features in the models.

The geometries are then meshed using unstructured spatially variable adaptive grid, capable of tracking free-form entities such as NURB.

Table 1
Length to Diameter Ratio Adopted in This Investigation

L/D	1.0 , m	5.0 , m	10.0 , m
0.067, m	16.7	83.3	166.7

Figure 1 represents the examples of the CAD geometries applied on this investigation, with respective finite element (FEM) mesh, where (a) is *L*/*D* of 16.7 model; (b) is *L*/*D* of 83.3 and (c) is *L*/*D* of 166.7.

The geometries are then meshed using unstructured spatially variable adaptive grid, capable of tracking free-form entities such as NURBS. In order to discretise the annular space inside of the tubing, and the surface walls of all geometric samples, an unstructured hybrid mesh consisting of triangle and tetrahedron elements are used and the mesh quality indicators are presented in Table 2.

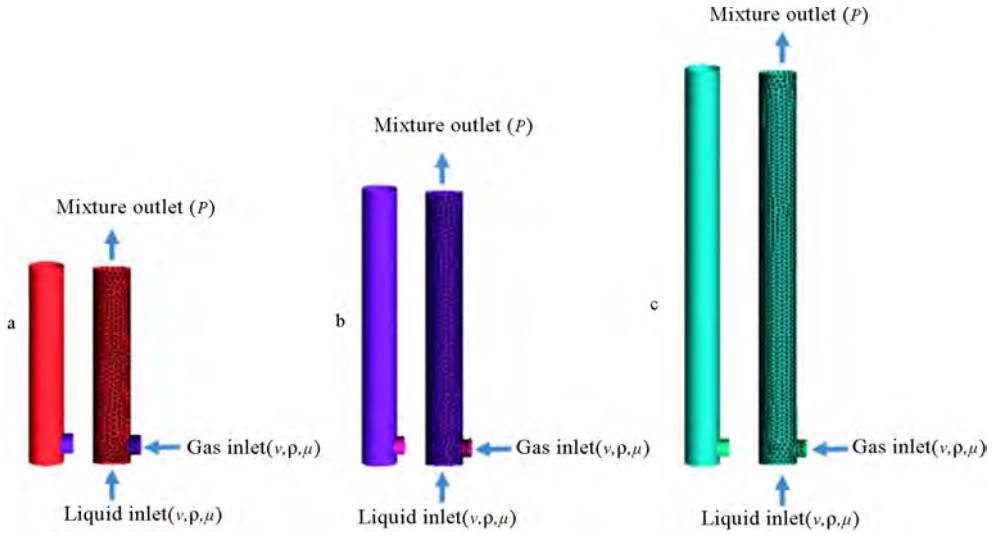

Figure 1
Computer-Aided-Design (CAD) and the Corresponding Finite Element Mesh for Selected Geometric Models of *L*/*D* Ratio (a) 16.7, (b) 83.3 and (c) 166.7

The mesh quality is characterised by the orthogonal quality ranges. The orthogonal quality ranges from 0 to 1, where values close to 0 correspond to low quality and values close to 1 are high quality and the maximum aspect ratio is required to be less than 5.[31] As show in Table 2, the mesh quality is in the range of the minimum required. Mesh qualities are improved by using high level diagnostic smoothening and modification algorithm in Integrated Computer Engineering and Manufacturing (ICEM) tool. Typical problems that may be associated with low mesh quality includes single, multiples edges, triangle boxes, overlapping elements, non-manifold and unconnected vertices.

Table 2
Sample Mesh Report

Quality/ratio	Minimum orthogonal quality	Maximum aspect ratio	Number of elements
L/*D* =16.7	0.793	3.29	60,117
L/*D* =83.3	0.677	2.94	73,199
L/*D* =166.7	0.987	1.8	61,304

Assumptions, Boundary and Initial Conditions

The transient two phase flow in vertical upward cylindrical pipe is assumed to be incompressible, immiscible, isothermal and with no mass transfer between the phases. Additionally, gravity and turbulence are taken into account, where the turbulence effects are evaluated by the use of the standard[32] and Renormalised group (RNG) models[33] and combined with the standard wall functions approach.

The inlet velocity for liquid phase is placed at the bottom of the tubing, while the gas inlet velocity was set at lower side of the tubing (see Figure 1). A Dirichlet boundary condition is applied in the inlet. The outlet boundary for the mixture is placed at the top of the tubing see Figure 1, where a pressure boundary condition (Neumam boundary condition) is applied at the outlet and it is set equal to zero Pascal, meaning that the outlet is open to the environment and the only pressure acting at the outlet is atmospheric pressure. The outer surfaces of the tubing are treated as wall with no slip[32] and no penetration, where denote the unit tangent on the boundary and unit normal to the boundary respectively. The initial conditions are presented in Table 3.

Table 3
Fluid Physical Properties and Initial Conditions

	Velocity,	Density	Viscosity,	Tension
Water	0.1	998.2	0.00103	0.073
Air	0.5-5	1.225	0.0000179	

2. NUMERICAL SIMULATIONS

The volume of fluid method, developed by Hirt[34] uses a phase indicator function, to track the interface between two or more phases. The indicator function uses values between 0 and 1 to distinguish between different fluids, which are considered as immiscible phases.

2.1 Governing Equations

The flow of two-phases in a tubing can be described by the general form of the momentum equation, constrained by the mass conservation equation. The momentum conservation equations can be written as:

$$\underbrace{\frac{\partial}{\partial t}(\rho U_j)}_{a} + \underbrace{\frac{\partial}{\partial z_j}(\rho U_i U_j)}_{b} = \underbrace{-\frac{\partial P}{\partial z_i}}_{c} + \underbrace{\frac{\partial}{\partial z_j}\mu\left(\frac{\partial U_i}{\partial z_j}+\frac{\partial U_j}{\partial z_i}\right)}_{d} + \underbrace{\rho g_j}_{e} + \underbrace{F_j}_{f} . \quad (2)$$

The mass conservation equation can be expressed as:

$$\frac{\partial \rho}{\partial t} + \frac{\partial}{\partial z_i}(\rho U_i) = 0 . \quad (3)$$

Where, ρ and U are the mixture density and mixture velocity respectively. In Equation 2, the term (a) represents the rate of increment in momentum per unit volume; (b) is the change in momentum due to convection; (c) is the pressure gradient; (d) represents the viscous and turbulent contributions; (e) is the gravitational forces and (f) represents the forces due to surface tension.

The surface tension is modelled by the continuum surface force formulation proposed by Brackbill et al.[35] For the cell lying at the interface, the mixture density, dynamic viscosity and the mixture velocity are related to the volume fraction and individual properties of phase *k*.

Thus:

$$\rho = \sum \alpha_k \rho_k , \quad (4)$$

$$\mu = \frac{\sum \alpha_k \rho_k \mu_k}{\sum \alpha_k \rho_k} , \quad (5)$$

$$U = \frac{\sum \alpha_k \rho_k U_k}{\sum \alpha_k \rho_k} . \quad (6)$$

For each phase present in the mixture, an additional transport equation, for its volume fraction needs to be included in the calculation, thus:

$$\frac{\partial}{\partial t}(\rho \alpha_k) + \frac{\partial}{\partial z_i}(\rho U_k \alpha_k) = S_k . \quad (7)$$

Where, S_k in Equation 7, is the source term.

For a Taylor bubble rising in a flowing liquid, the following elliptic equations are required as closure for the Reynolds Average Navier Stokes (RANS) equations:

$$\rho U_j \frac{\partial k}{\partial z_j} = \frac{\partial}{\partial z_j}\left(\frac{\mu_t}{\sigma_k}\frac{\partial k}{\partial z_j}\right) + \mu_t \frac{\partial U_j}{\partial z_i}\left(\frac{\partial U_i}{\partial z_j}+\frac{\partial U_j}{\partial z_i}\right) - \rho\epsilon , \quad (8)$$

$$\rho U_j \frac{\partial \varepsilon}{\partial z_j} = \frac{\partial}{\partial z_j}\left(\frac{\mu_t}{\sigma_\varepsilon}\frac{\partial \varepsilon}{\partial z_j}\right) + C_1 \frac{\partial U_j}{\partial z_i}\left(\frac{\partial U_i}{\partial z_j}+\frac{\partial U_j}{\partial z_i}\right) - C_2 \frac{\varepsilon}{k}\rho\epsilon . \quad (9)$$

Where k is the turbulent kinetic energy; ε is the dissipation rate of k, μ_t is turbulent viscosity. σ_k, σ_ε, C_1, C_2 are constants with the following values 1.00, 1.30, 1.44 and 1.92 respectively.[10]

In order to estimate the inlet values of the turbulent kinetic energy k and the dissipation rate, ε the following equations proposed by launder and Spalding[32] are used.

$$k_{in} = \frac{3}{2}\left(\frac{0.16}{Re^{\frac{1}{8}}}\right)^2 U_{in}^2 , \quad (10)$$

$$Re = \frac{\rho U_{in} D}{\mu}, \quad (11)$$

$$\varepsilon_{in} = \frac{2}{D} k_{in}^{\frac{3}{2}} . \quad (12)$$

Where, U_{in} is the superficial velocity at the inlet in m/s, R_e is the Reynolds number, while ε_{in} is the corresponding dissipation rate.

The k-ε model used in this numerical simulation is semi-empirical model which has been developed for single phase. Scarcity of knowledge exists about their behaviour close to the gas-liquid interface, where there is discontinuity in the values of density and viscosity.[36- 37]

2.2 Solution Algorithm

Numerical simulation based on the finite volume method was used to solve the continuity equation (Equation 3), momentum equation (Equation 2) and transport equation (Equation 7). The domain is discretised into a finite set of control volumes or cells. Each transport equation is discretised into algebraic form by expressing the variation in the dependent variable and its derivatives, using interpolation profiles, in terms of the grid point values.[38]

Material properties, velocities are calculated at cell centers and face values are interpolated in terms of local and adjacent cell values.[31]

Semi-implicit method for pressure-linked equations algorithm developed by Patankar and Spalding[39] is applied. Additionally, under relaxation factors on pressure, momentum and turbulent kinetic parameters are set to be 0.30, 0.70 and 0.80 as suggest by ANSYS.[31]

2.3 Grid Convergence

Mesh or grid independence study is carried to determine this optimum point where a fairly accurate solution for the problem is found at the expense of least computational resources

To establish the convergence of the scheme to a mesh-independent solution, a mesh independence study is carried out to determine the optimum number of elements where a fairly accurate solution is found. Unsteady state air-water flow in vertical upward tubing of 0.067 m diameter and 1.0 m length is computed using unstructured mesh, where we start with a coarse mesh of 60,117 elements and increase the mesh density successively. Thus, the computations are done for 60,117, 66,460 and 74,570 elements respectively. The meshes were tested with an inlet flow conditions of air superficial velocity of m/s, and water superficial velocity of m/s and the mesh report is presented on Table 4. Radial profile of the axial velocity on the Taylor bubble nose for each mesh density is presented. From Figure 3, we found that solutions are indistinguishable for mesh densities greater than 66,460.

Table 4
Mesh Information

	Coarse mesh (a)	Medium mesh (b)	Fine mesh (c)
Number of elements	60,117	66,460	74,570
Number of nodes	61,184	67,584	75,755
Minimum orthogonal quality	0.79	0.84	0.93

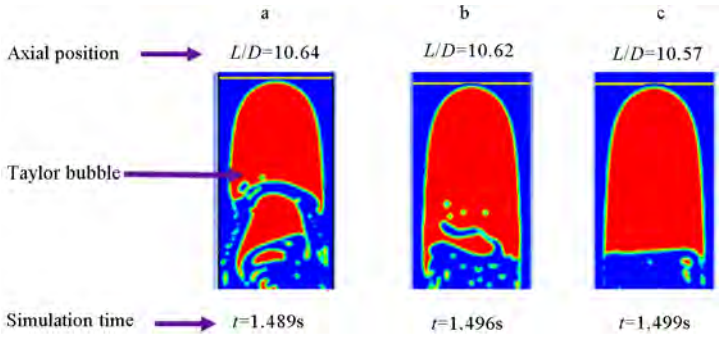

Figure 2
Spatial and Transient Coordinates of the Reference Slit (Yellow Line) Along the Taylor Bubble Nose for Axial Velocity Computation at Different Mesh Densities. (A) Is the Taylor Bubble in Coarse Mesh, (B) Is the Taylor Bubble in Medium Mesh and (C) Is the Taylor Bubble in the Fine Mesh

For a coarse mesh a the axial velocity at Taylor bubble nose was computed on position of L/D =10.64 and simulation time of 1.499 s, and for a medium mesh, the axial velocity was calculated on position on position of L/D =10.62 and simulation time of 1.496 s while for the fine mesh, a position of L/D=10.57 and simulation time of 1.489 s were used.

2.4 Numerical Validation Method

To validate the approach developed in this work, a study on transient air-water flow in vertical upward was conducted and compared with the experimental measurement by Polonsky et al.[40]

The experimental test section of the rig consisting of 0.025 m diameter and 4.0 m length, was replicated numerically by use of CAD tool and meshed in ICEM CFD. The numerical tests were carried out at axial distance of the test sections of *L*/*D* of 13.08; 13.12; 13.16; 13.2 respectively. Inlet air superficial velocity of m/s was assigned at inlet, while water was assumed stagnant inside the pipe. In order to ensure that the reading is accurate, a fine grid mesh consisting of 227,444 elements were used. 2*D* geometry mesh representation of the fluids inlet section is showed in Figure 4 (a) and the corresponding mesh quality histogram is presented in (b), where a minimum orthogonal quality of 0.56 was obtained.

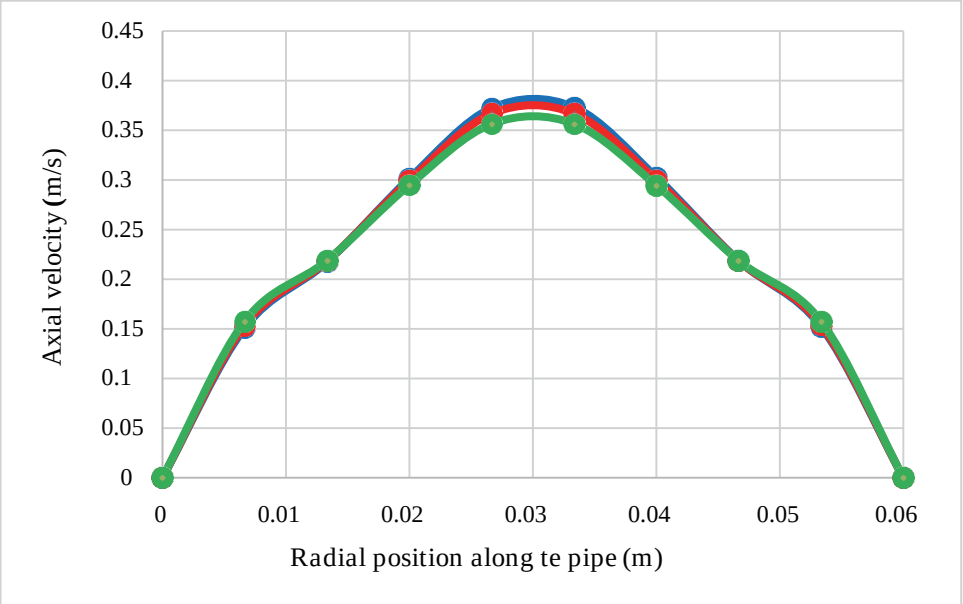

Figure 3
Influence of Mesh Size on Numerical Results

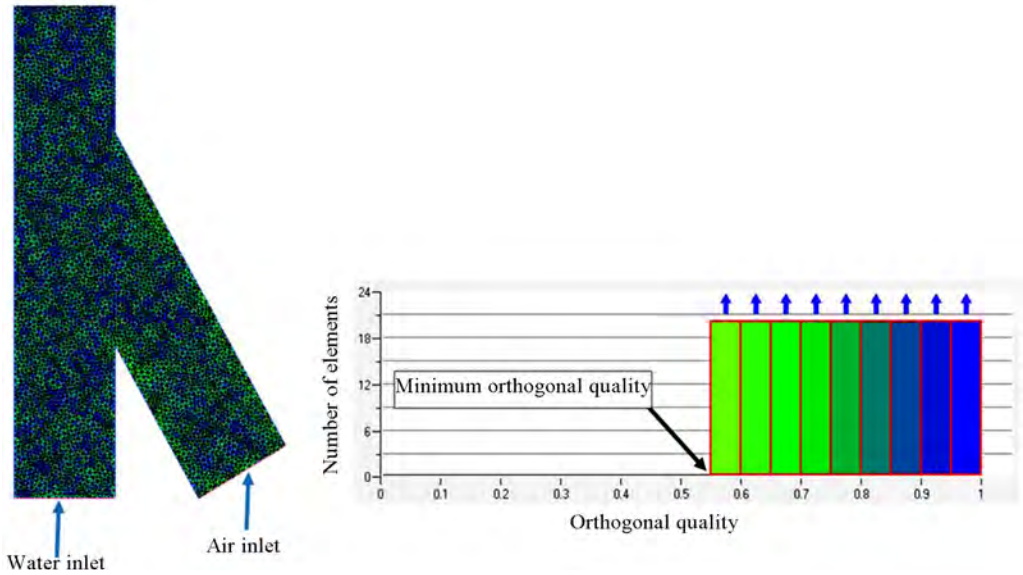

Figure 4
2*D* Representation of the Geometric Mesh (a) and Respective Mesh Orthogonal Quality (b)

Figure 5 shows a qualitative comparison between the numerical and experimental data obtained from Pololonsky et al.[40] The velocity profiles are normalized by the maximum velocity .

Qualitatively, the numerical solution compare well to the experimental data in all aspects as noticed in Figure 5. The axial velocity ahead of the nose of Taylor bubble was normalised by dividing the current axial velocity by the maximum axial velocity.

The trend of results obtained is observed to be within reasonable degree of accuracy in comparison with the

experimental results. This can be attributed to the very high mesh refinement used in the numerical simulation.

The predicted axial velocity profiles ahead of the Taylor bubble were in good agreement with the observed data. Thus, it can be concluded that, in spite of some deviations, the present simulation can generally predict the axial velocity profiles ahead of the Taylor bubble.

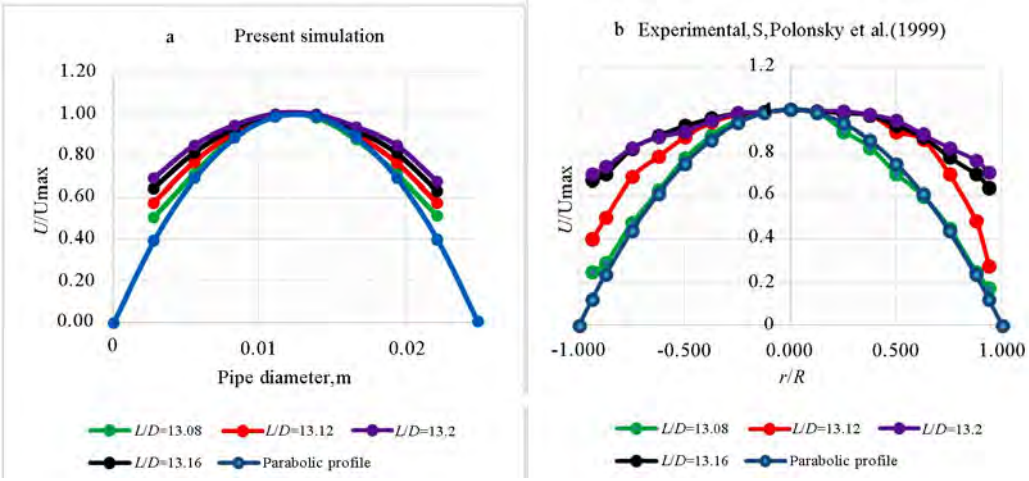

Figure 5
Comparison Between Present Simulation (a) With the Experimental Data From Polonsky et al.[40] Measurement (b), of the Velocity Profiles Ahead of the Taylor Bubble Air-Water Two-Phase Flow in Vertical Upward in the Tubing of 0.025 m of Diameter and 4 m

3. RESULTS AND DISCUSSION

3.1 Influence of Inlet Geometry Configuration on Bubbles Evolution and Devolution Close to the Injection Point

The effect of gas injection geometry on bubble size evolution is evaluated. 2*D* geometric mesh representation is shown in Figure 6(a), and the respective mesh orthogonal quality is presented on (b). The air inlets are three porous of 0.002 m ID each, while the water inlet is 0.06 m ID. Additionally, the influence of air inlet superficial velocity has been assessed, where values of 1.5, 3.0 and 5 m/s respectively, where assigned at the air inlet. Additionally, a comparison between single air injection and porous air injector were performed.

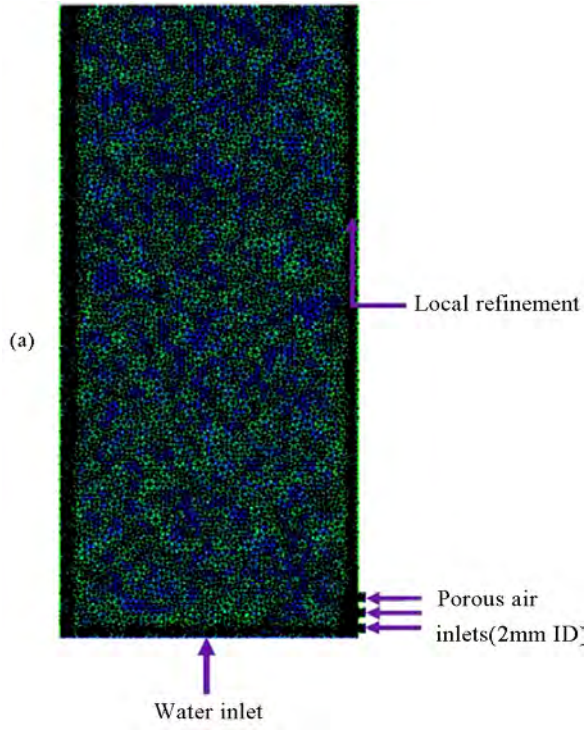

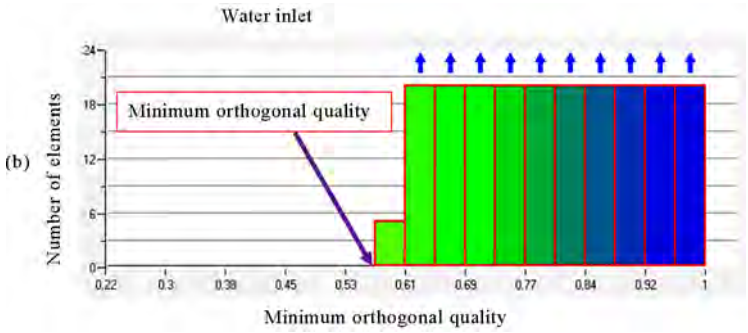

Figure 6
2*D* Representation of the Geometric Mesh (a) Respective Mesh Orthogonal Quality (b). The Mesh Has Been Refined Along the Pipe Inlets and the Pipe Internal Walls as Shown in (a)

3.1.1 Effect Air Inlet Superficial Velocity on Bubbles Dynamics

The computed transient evolution of air bubbles (red colour) is illustrated in Figure 7. By varying the air inlet superficial velocity from 1.5 to 5 m/s, while keeping the water inlet velocity of 0.1 m/s constant, the effect of geometry configuration was critically evaluated. As can be seen from Figure 7, the bubbles volume increases with increasing air superficial velocity, which is also in agreement with previous study of Shao et al.[41] for similar systems. The influence of low air injection rate is also reflected in bubbles residence time, where we see that for small bubbles size the residence time is higher compared to high injection rate. Moreover, the bubbles volume expansion rate increase with air inlet superficial velocity. In all range of air inlet superficial velocities, the air bubbles present irregular shape and with deformation. Low air injection rate results in low bubble size formation and high residence time, while high air injection rate provides high bubbles size and low residence time.

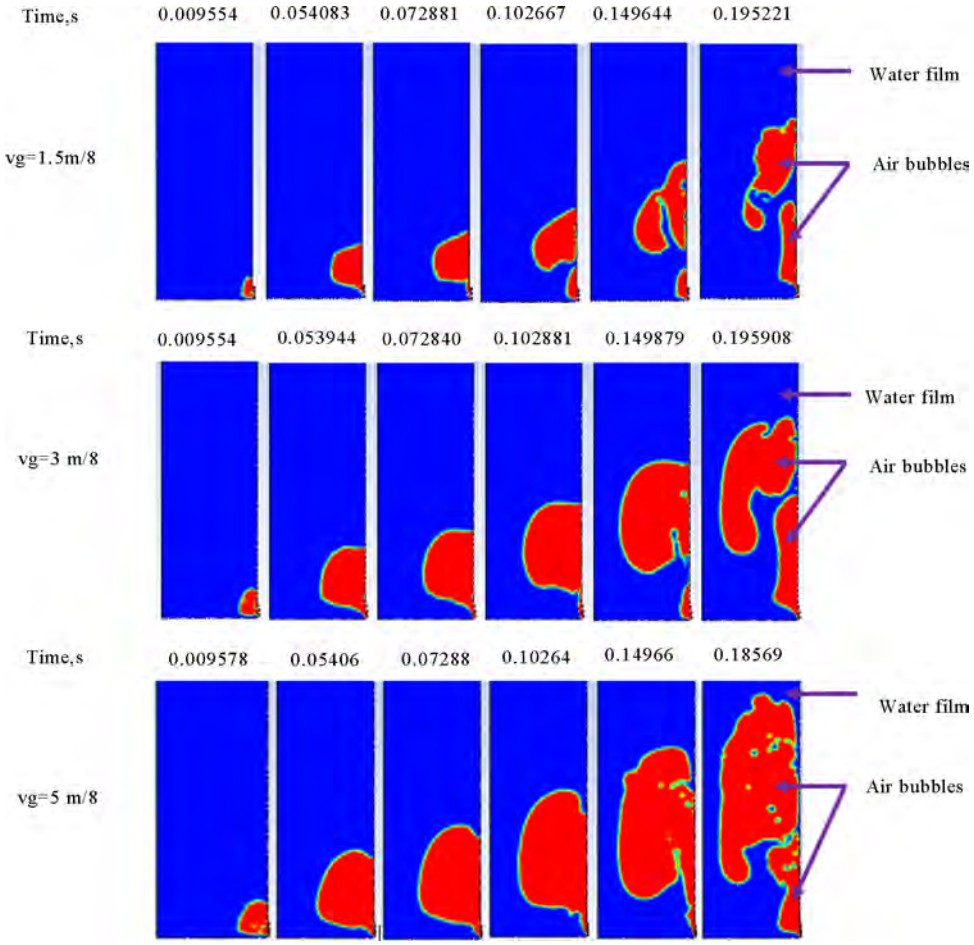

Figure 7
Air Bubbles (Red) Distribution Close to the Inlet as Function of Inlet Superficial Velocities at Constant Water Superficial Velocity of 0.1 m/s

3.1.2 Comparative Analysis of the Air Injector Configuration's Role on Bubbles Dynamics Close to the Injection Point

The influence of air inlet configuration on air bubble evolution is addressed, by comparing the transient evolution of bubbles with porous injectors and single injector respectively.

As noticed from Figure 8, the size of the air inlet affects the bubbles size evolution. Larger bubbles are formed at the injection point region for single nozzle compared to porous nozzle for almost similar residence time. The increase in orifice diameter, produce larger bubbles sizes with the tendency to for a Taylor bubble. The bubbles expansion rate is higher in single injector configuration compared to the porous injectors while the bubble deformation is noticed in the porous injectors compared to single injector.

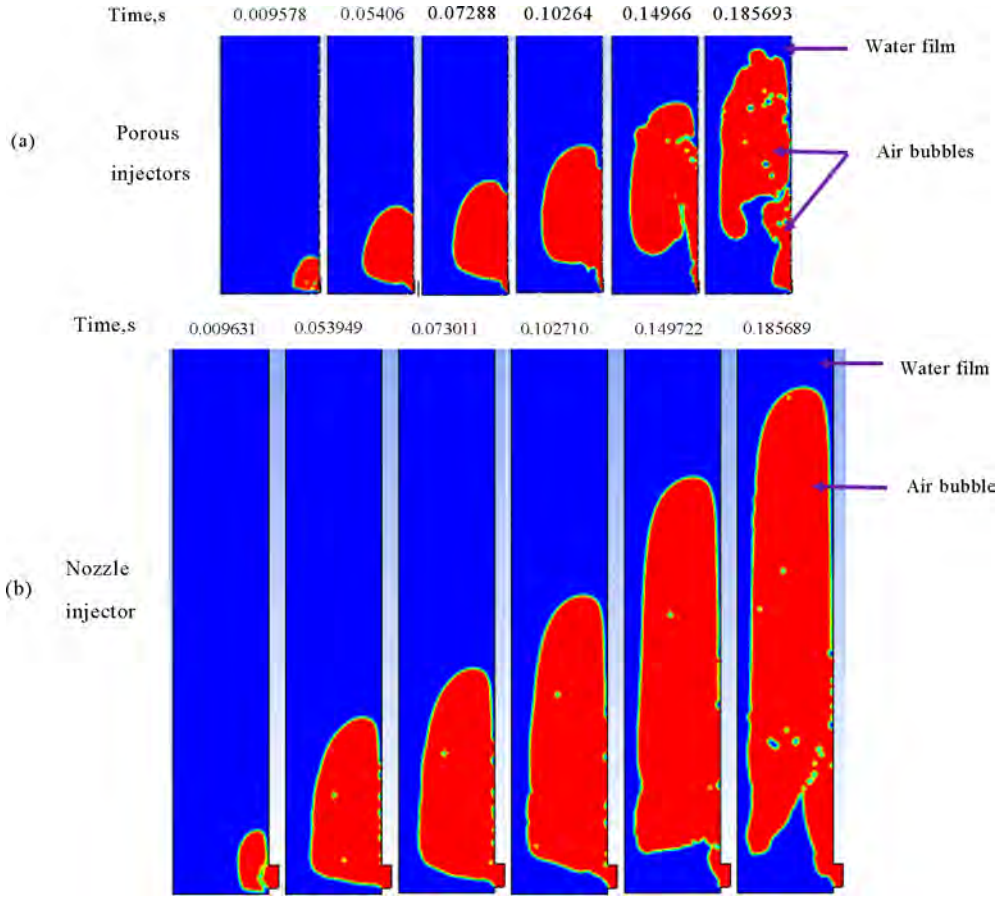

Figure 8
Numerical Computation of Transient Air Bubble Expansion (Red Colour) for (a) Porous Injectors Configuration of 0.002 m ID Each, (b) Single Injector Configuration of 0.02 m ID. The Inlet Air Superficial Velocity is 5 m/s While 0.1 m/s Is for Water Inlet Superficial Velocity

3.2 Effect of Air Inlet Superficial Velocity on Flow Regime Structure

In order to investigate the effect of air inlet superficial velocity on the flow regime structure, liquid superficial velocity of 0.1 m/s and varying gas-lift injections superficial velocities of 0.5, 1.0 and 1.5 m/s were assigned on *L*/*D* ratio of 16.7.

Visualisation of the phase distribution can be observed with distortions on the phase interface, where bullet-shaped bubbles are identified in all cases. The red colour in Figure 9 represent 100% air or 0% water and blue color represent 0% air or 100% water.

According to She et al. and Hui Liu,[42- 43] the churn flow regime is characterised by the existence of relatively large deformed bubbles agitating the flow and producing strong local turbulence when increasing the gas superficial velocity. Because of the high gas velocity, a wave or ripple motion is observed at the bubble tail with the tiny gas bubbles entrained in the liquid slug.

In all cases the coexistence of slug, churn and annular regime is observed, and this behaviour is in agreement with Imada et al.; Taitel et al.; Sharaf et al.; Kaji et al.; Ansari and Azadi; Johansen et al.; Mayor et al.; Szalinski et al.[6- 7, 14, 26-27, 44-46]

The annular flow results observed in Figure 9(c), indicates the presence of continuous gas phase in the central core of the tubing with the liquid phase being displaced to form an annulus between the tubing wall and the gas phase.

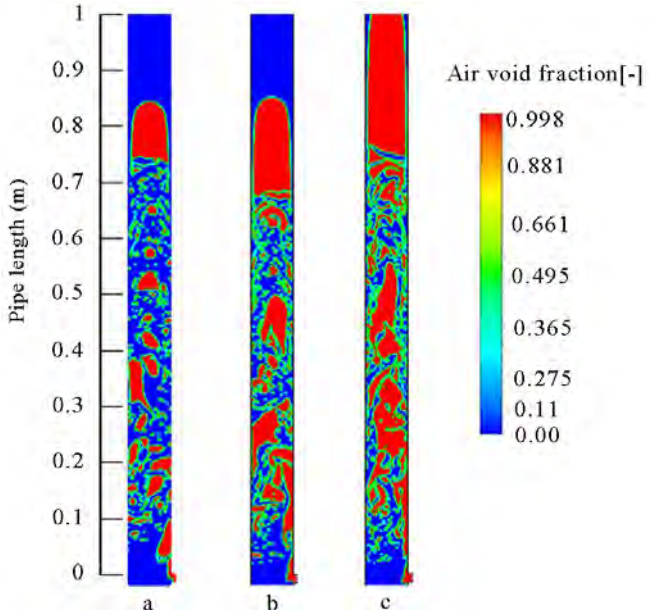

Figure 9
Influence of Gas-Lift Gas Injection Superficial Velocity on Air-Water Flow Structures for a Pipe *L/D* Ratio of 16.7. (a) Represents Inlet Gas Superficial Velocity of 0.5 m/s, (b) Is Assigned for Inlet Gas Superficial Velocity of 1.0 m/s, While (c) Shows the Inlet Gas Superficial Velocity of 1.5 m/s. The Liquid Inlet Velocity Was Maintained Constant And Equal to 0.1 m/s. The Red Color Represents the Air Volume Fraction and Blue Color Represents the Water Phase Volume Fraction

As observed in Figure 9, increasing the gas superficial velocity caused the bubble density to become higher and the bubble size to become larger. This gradual change in the fluid structure, leads to the development of annular flow where the gas phase becomes the continuous phase, flowing in the core section of the tube, surrounded by the liquid flowing as a film in the annular space between the gas phase and tube wall. Figure 9, shows also that the liquid film thickness around the leading Taylor bubble decrease with increase of air inlet superficial velocity. This observation is in agreement with Sasaki et al., Morgado et al., Wang et al., Icardi et al.[15, 47-49]

3.3 Hydrodynamics of Taylor Bubble and Its Surrounding Liquid Film

3.3.1 Taylor Bubble Shape and Velocity Field Structure in Flowing Water Film

Figure 10 shows the 2*D r-z* cross-sections of the Taylor bubble and the corresponding, velocity field vectors where four main regions are identified. A is a wake region, **B** is Taylor gas stream, C is the hemispherical or prolate-hemispheroidal nose and **D** is a falling liquid film region. In the region **A**, it is possible to visualise some liquid being dragged upward by the gas; in the region **B** there is uniform velocity field, while deviations of velocity field is observed in region **C** with near tendency of uniformity faraway for region **C**, falling film can be observed moving downward in the regions **D**.

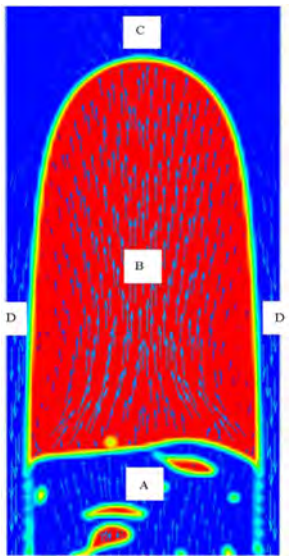

Figure 10
***r-z* Cross-Sectional View of a Taylor Bubble Shape in Flowing Liquid Film and Corresponding Velocity Field Vectors**

3.3.2 Influence of Pipe Length on the Radial Profile of the Axial Velocity Along the Taylor Bubble and Around It

The axial velocity fields were plotted for radial positions at different axial distances in regions (A), B) and (C) presented in Figure 10. The corresponding results of the radial component of the axial velocities profiles in regions (A), B) and (C) for *L/D* ratios of 16.7, 83.3 and 166.7, are presented in Figures 11, 12, and for air inlet superficial velocity of 0.5 m/s; and water inlet superficial velocity of 0.1 m/s respectively.

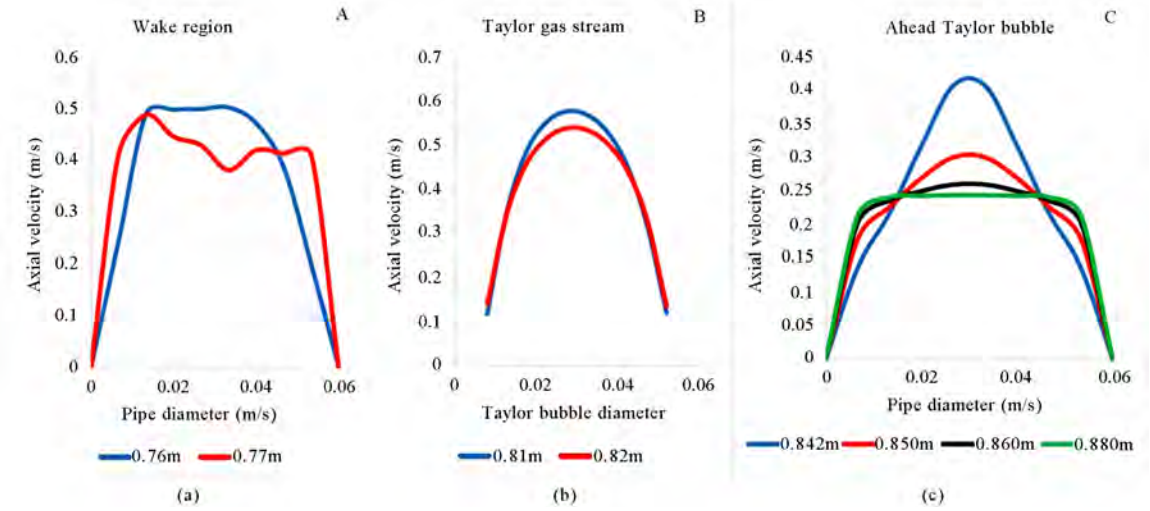

Figure 11
Radial Distribution of the Axial Velocity at Different Axial Positions in (a) Region A Below the Taylor Bubble, (b) Region B (Inside the Taylor Bubble) and (c) Above Region C (Taylor Bubble Nose) for a Geometry of *L/D* of 16.3 and 0.5 m/s Gas Initial Velocity. The Blue Line in c, Represents the Radial Profile of the Axial Velocity at Taylor Bubble Nose

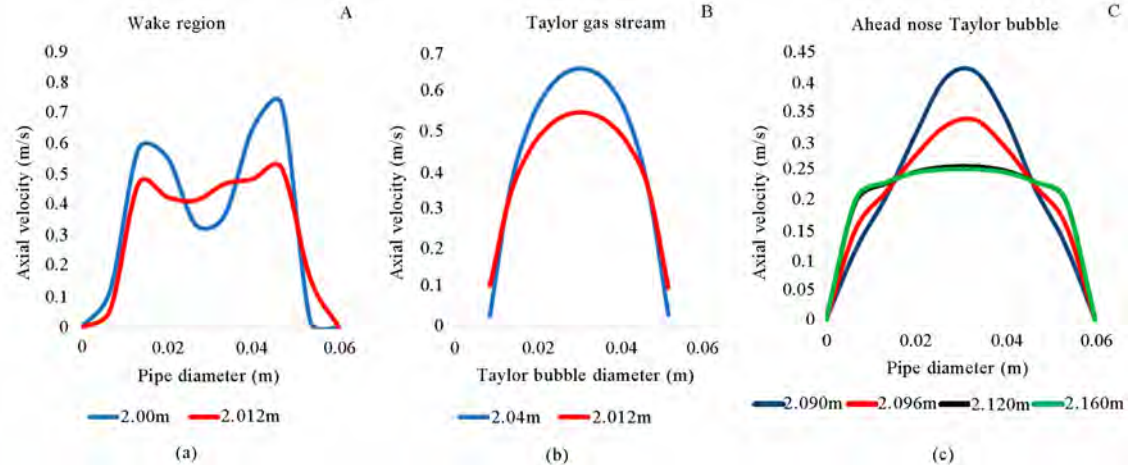

Figure 12
Radial Distribution of the Axial Velocity at Different Axial Positions in (a) Region A Below the Taylor Bubble, (b) Region B (Inside the Taylor Bubble) and (c) Above Region C (Taylor Bubble Nose) for a Geometry of L/D of 83.3 and 0.5 m/s Gas Initial Velocity. The Blue Line in c, Represents the Radial Profile of the Axial Velocity at Taylor Bubble Nose

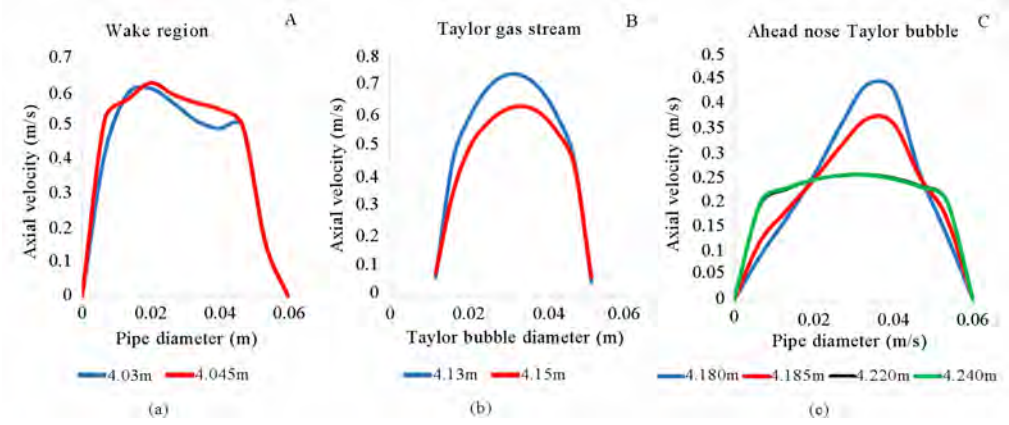

Figure 13
Radial Distribution of the Axial Velocity at Different Axial Positions in (a) Region A Below the Taylor Bubble, (b) Region B (Inside the Taylor Bubble) and (c) Above Region C (Taylor Bubble Nose) for a Geometry of L/D of 166.7 and 0.5 m/s Gas Initial Velocity. Blue Line in c, Represents the Radial Profile of the Axial Velocity at Taylor Bubble Nose

In the wake region **A**, it can be observed a fluctuation on the radial profile of axial velocity due to vortexes, with no well-defined boundary. This trend is observed in all *L*/*D* ratio domains as shown on Figures11-13. Wang et al. (2014) [48] have observed similar profile when they investigated experimental the characteristics of slug flow in vertical narrow rectangular channel.

A fully parabolic profile is observed on *L*/*D* ratio of 16.6 and 83.3 respectively, while, a distortion and off-centered in the axial velocity profile is observed on *L*/*D* ratios of 166.7 in the Taylor gas stream region **B**.

At the Taylor bubble nose (blue line on region c), a parabolic profile of the axial velocity is observed on *L*/*D* ratio of 16.7 and 83.3 while for *L*/*D* ratio of 166.7 we see a distortion and eccentricity in the axial velocity profile. Ahead the Taylor bubble, flattening of the axial velocity profile is observed in all geometry domains. The influence of liquid load on the nose of the Taylor bubble is noticed in region **C** on *L*/*D* ratio of 166.6 where there is no appreciable difference on velocity profile in axial positions ahead the nose of Taylor bubble (Figure 13, c) in comparison with *L*/*D* ratio of 83.3 (Figure 12, c) and *L*/*D* ratio of 16.7 (Figure 11, c) respectively.

3.3.3 Estimation of Taylor Bubble Velocity and Its Length in Continuous Slug Flow

The computed dynamic evolution of Taylor bubble rising velocity as well its elongation on time are presented in Figures 14 and 15 respectively. The bubble rising velocities were determined by the relations: Where is the distance traveled in between two positions of the Taylor bubble nose and is the corresponding time interval. The distance travelled by the nose of the Taylor bubble were measured for each time step computed, while the lengths of the bubbles were estimated by measuring the distance between the Taylor bubble nose and its wake region for every simulation time. The distance traveled by the nose of Taylor bubble is plotted as function of time for *L*/*D* geometries of 16.7 (a), 83.3 (b) and 166.7 (c) respectively. The slope of the linear trend-line on Fig. 14 represents the Taylor bubble rising velocity. From this, it was found that the Taylor bubble average velocity is 0.4106 m/s for *L*/*D* =16.7, 0.4245 m/s for *L*/*D* =83.3 and 0.4509 m/s for *L*/*D* =166.7 respectively. In the range of the pipe length, the Taylor bubble rising velocity increases with exponential power law of the pipe length as follows:

$$U_B = 0.4051 * e^{\left(0.006\frac{L}{D}\right)}. \quad (13)$$

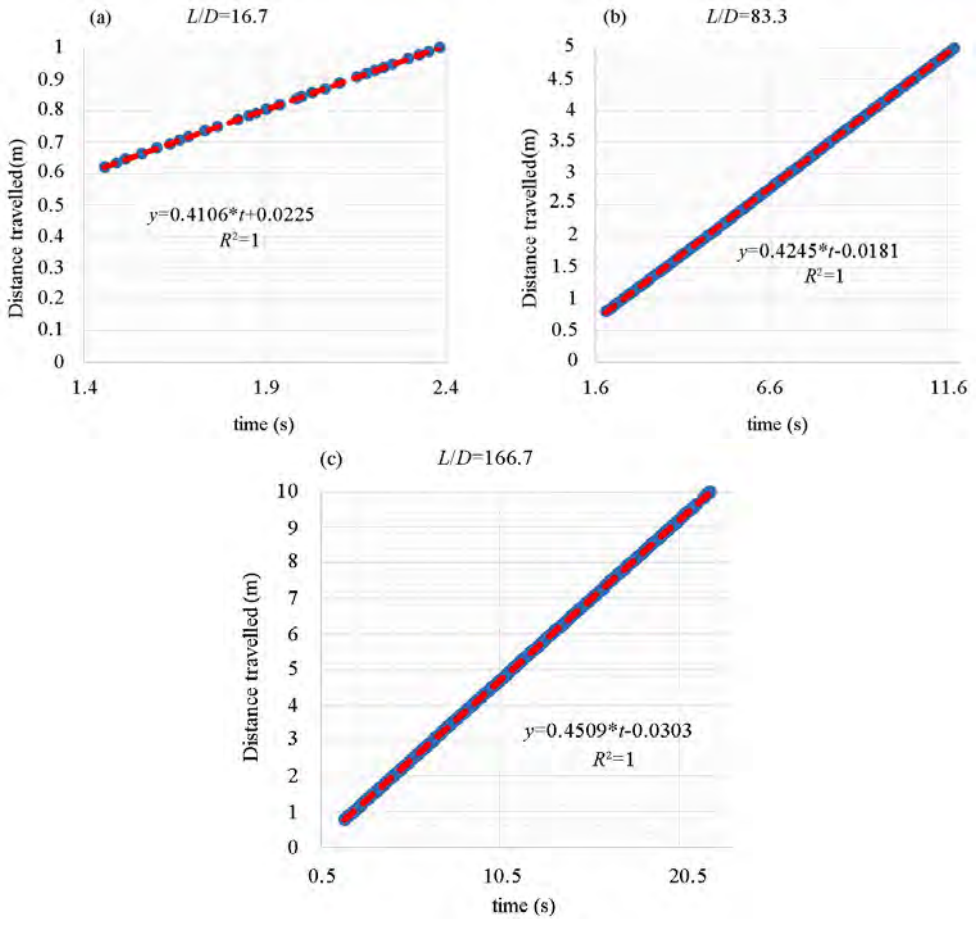

Figure 14
Consecutive Leading Taylor Bubble Nose Position as Function of Time for Geometry Domains of *L*/*D* Ratio of 16.7 (a), 83.3 (b) and 166.7 (c). For All *L*/*D* Ratios, the Liquid Superficial Velocity Is 0.1 m/s, and Gas Superficial Velocity Is 0.5 m/s

Figure 15, displays the estimated Taylor bubble length as function of time for *L*/*D* ratios of 16.7, 83.3; and 166.7 correspondingly. Different trends are observed in all *L*/*D* ratios. In (a) we see positive increment of the Taylor bubble length on time suggesting an expansion of the leading Taylor bubble on time. The profile on (b) is apparently showing aperiodic oscillation on time while in (c), we see a tendency of the parabolic profile of leading Taylor bubble length on time having a maximum value.

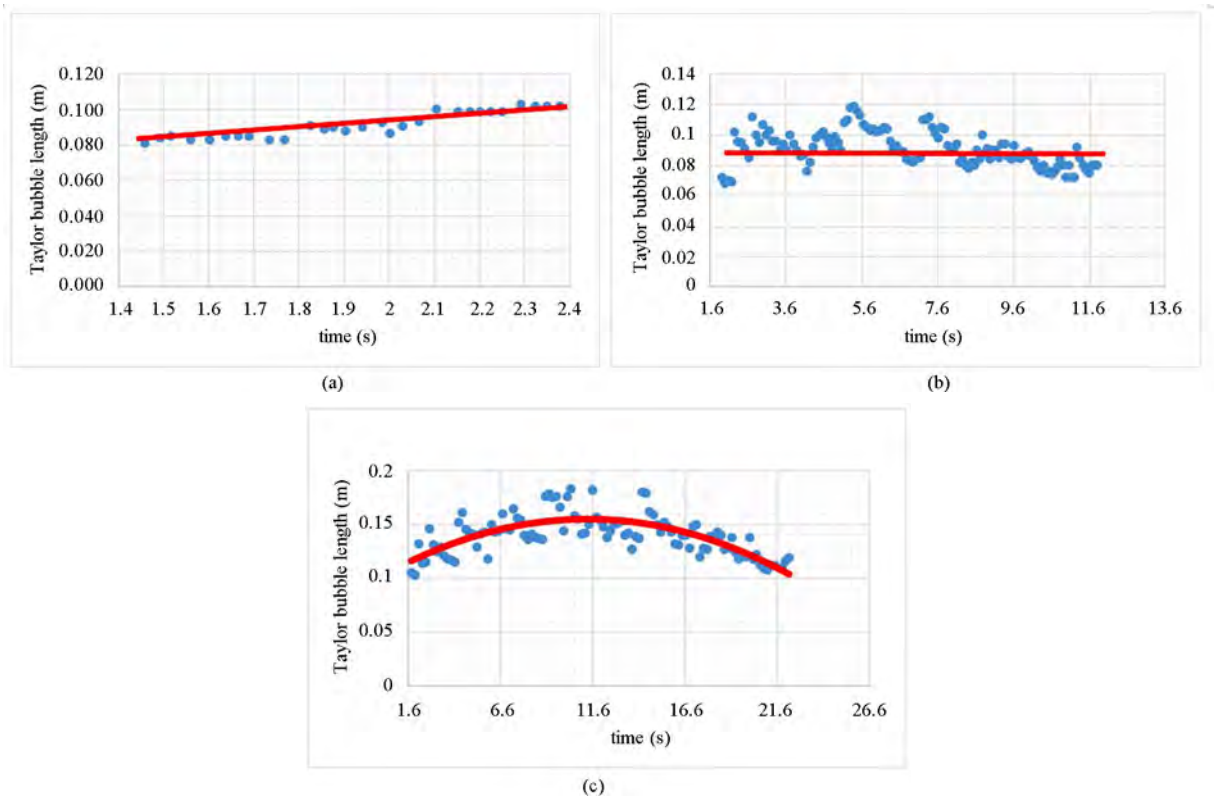

Figure 15
Plots of Taylor Bubble Length Versus Time for (a) *L*/*D* Ratio of 16.7, (b) L/D ratio of 83.3 and (c) *L*/*D* Ratio of 166.7. For All *L*/*D* Ratios, the Liquid Superficial Velocity Was 0.1 m/s, and Gas Superficial Velocity Was 0.5 m/s Respectively

3.3.4 Air Bubbles Breakup and Coalescence Evolution Along the Pipe Length

Coalescence, defined as the process by which two or more bubbles merge during contact to form a single daughter bubble, is visible along the pipe length as shown on Figure16 far ahead of the injection point on other hand, bubble breakup mechanism is observed and noticed close to the injection point.

The slug flow regime characterised by the existence of large coalescent cap bubble that nearly fully occupies the pipe cross-section with hemispherically shaped tops and flattened tails were observed.

From Figure 16, we see small gas bubbles are entrained in the tail of Taylor bubble. Distorted nose of trailing bubble is observed as it is traveling in the wake region of the leading bubble; acceleration of the trailing bubble and consequent coalescence with the leading bubble is also observed; showing the characteristic of unstable slug flow. Far from the injection point, the density of small bubbles is higher and the coalescence rate is noticed compared to breakup rate.

3.3.5 Influence of Pipe Length on Water Flow Field in Front of the Taylor Bubble

The radial distribution of the axial velocity are normalised by the maximum velocity at the center line of the pipe diameter. The theoretical parabolic distribution is plotted together with the numerical solution results. From Figure 17, we see that by increasing the pipe length, the radial profile of the axial velocity tends to be parabolic and this trend is more pronounced on *L*/*D* ratio of 166.7 compared to *L*/*D* of 83.3 and 16.7 respectively. This profiles, advocate that the axial velocity profile in the liquid film ahead the leading Taylor bubble is influenced by the pipe length. Comparable profiles were observed by Polonsky et al., Santos and Pinheiro, Wang et al.[23, 40, 48] respectively, where they found that the velocity profile is well fitted with one-seventh power-law, despite they have used fixed pipe length. From this results one can be assured that the *L*/*D* ratio of 166.7 is not sufficient to achieve the fully developed flow of the liquid ahead the leading Taylor bubble.

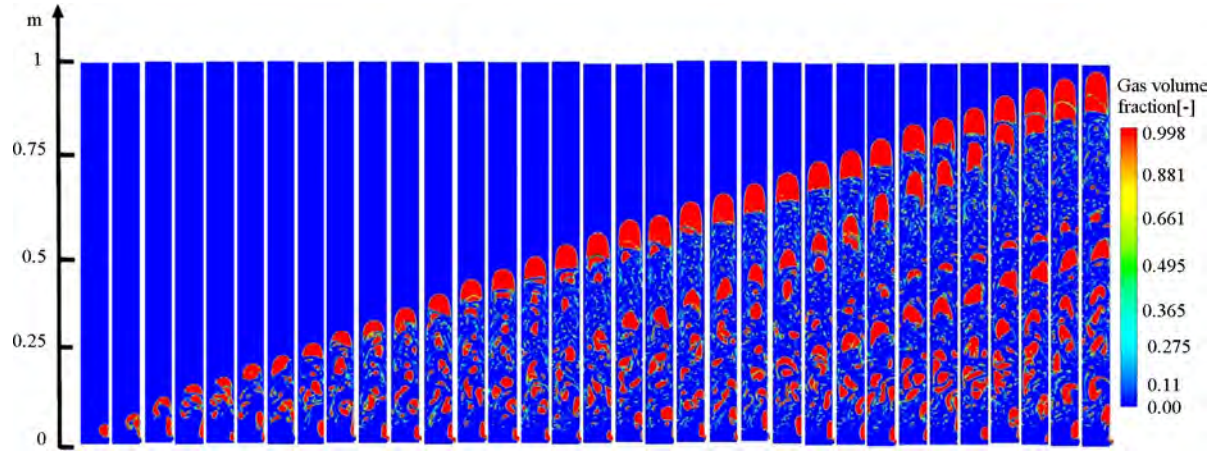

Figure 16
Sequential Images of the Bubbles Coalescence and Breakup Mechanisms, on Geometry Domain of *L*/*D* Ratio of 16.7, Liquid Superficial Velocity of 0.1 m/s, and Gas Superficial Velocity of 0.5 m/s. Red Colour Represents the Gas Bubbles and the Blue Is the Water Phase

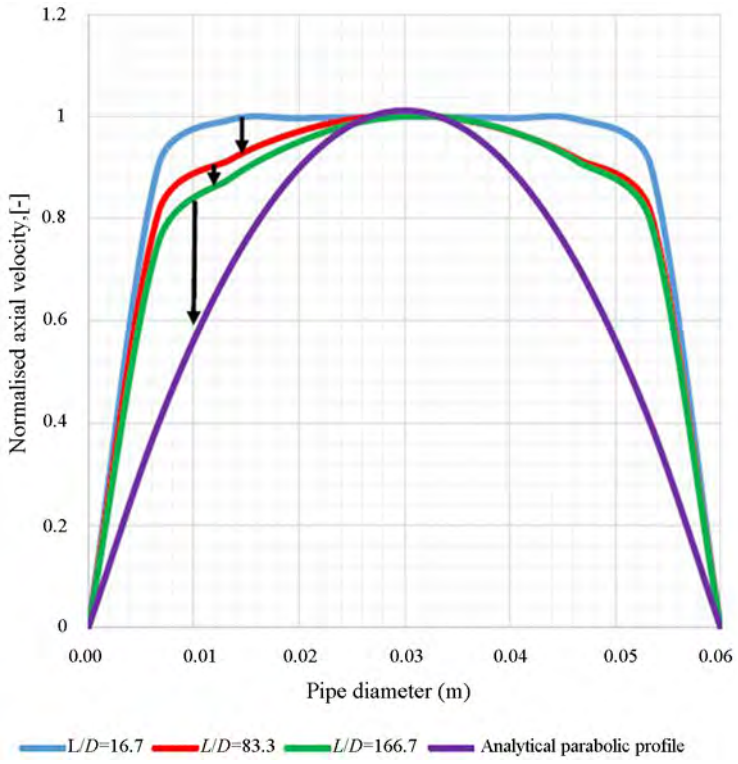

Figure 17
The Average Axial Liquid Velocity Distributions Above the Taylor Bubble Nose for Geometry Ratio of 16.7, 83.3 and 166.7 for Air Inlet Superficial Velocity of 0.5 m/s, and the Liquid Superficial Velocity of 0.1 m/s Are Presented. Additionally, the Theoretical Parabolic Distribution Is Plotted Together With the Numerical Solution

The theoretical power-law for axial velocity described by Equation 14 is compared with the numerical solution as presented in Figure 19.

$$U_n = \frac{U}{U_{\max}} = \left(1 - \frac{r}{R}\right)^{\frac{1}{n}} \quad . \tag{14}$$

The power law of normalised axial velocity profile in the range of the *L*/*D* ratios is reasonable represented as:

$$U_n = \begin{cases} \left(1 - \frac{r}{R}\right)^{\frac{1}{15}} \text{ for } {}^{L}/_{D} = 16.7; n = 16 \\ \left(1 - \frac{r}{R}\right)^{\frac{1}{8}} \text{ for } {}^{L}/_{D} = 83.3; n = 8 \\ \left(1 - \frac{r}{R}\right)^{\frac{1}{6}} \text{ for } {}^{L}/_{D} = 166.7; n = 6 \end{cases} . \tag{15}$$

Figure 19 shows comparison of the devolved analytical solutions based on equation 14 using different values of exponents as indicated in Equation (15). For

different values of tested on L/D =16.7 for example, the minimum relative error between the numerically computed normalised axial velocity and analytically obtained values, is obtained when the value of n=16. For this error analysis several values of n=14, 15, 16, 17, 18, 19 and 20 were tested for L/D =16.7. Similar tests were performed for L/D =83.3 and L/D =166.7 with the exponent ranging from 6 to 9 for L/D =83.3 and 4 to 7 for L/D =166.7 respectively.

It is postulated that the graphic of versus will collapse on to the parabolic solution for higher values of L/D. This has not been numerically tested in this manuscript.

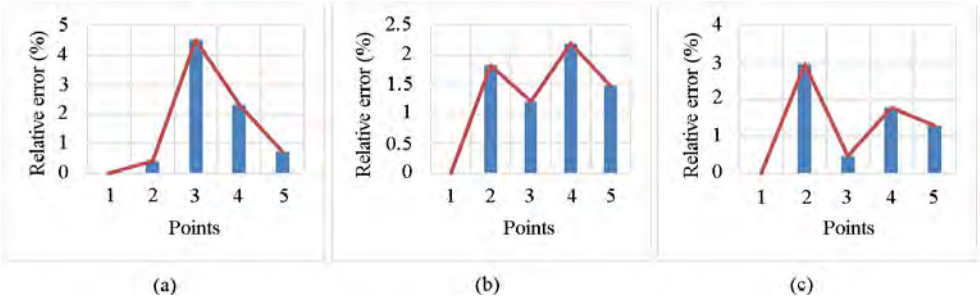

Figure 18
Least Relative Error Analyses for Best Fit Exponent n in the Power Law Equation With the Corresponding Numerical Solution as Shown in Figure 19. In (a) n=16 and L/D=16.7; (b) Stands for n=8 and L/D=83.3; (c) It Is for n=6 and L/D=166.7

Figure 18, shows the summary of the least relative errors obtained for each of the cases presented. It is therefore hereby concluded that Equation 14 can be effectively used to predict the relationship between the normalised velocity and the pipe diameter.

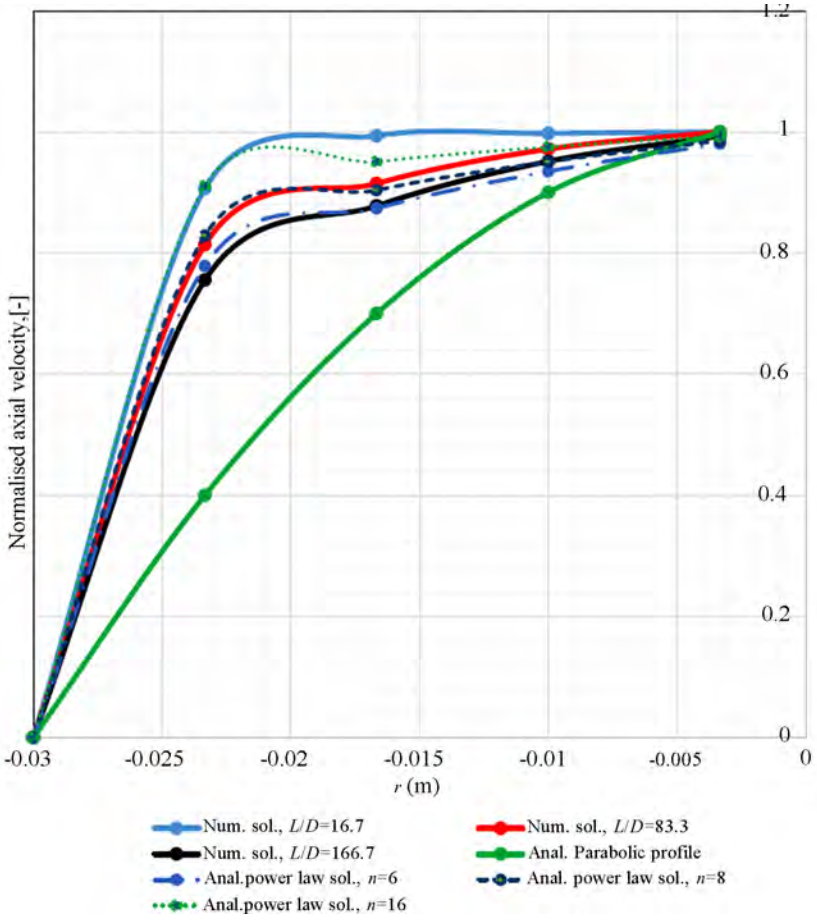

Figure 19
Comparison Between Present Simulation With the Theoretical Solution (Equation 14) of the Axial Velocity Profile Ahead the Taylor Bubble Nose

CONCLUSION

For a fixed pipe diameter of 0.06 m investigated in this work, the following conclusions are addressed.

Aperiodic behaviour in time and space dictates the complexity of continuous and unstable two phase slug flow. The breakup and coalescence mechanisms are observed along the pipe length.

Pipe length may influence the bubbles expansion as they rise along the pipe. The single nozzle geometry of the air inlet is source of large bubbles generation at the injection zone and those bubbles travel along the pipe breaking up and coalescing successively.

The porous injection configuration produces small bubbles size compared to a single gas injection configuration even at higher gas injection rate.

Average axial velocity of the leading Taylor bubble of 0.4106 m/s, 0.4245 m/s and 0.4509 m/s were obtained for L/D ratios of 16.6, 83.3 and 166.7 respectively.

The eccentricity distributions of axial velocity in leading Taylor bubble stream and on its nose are perceived from L/D ratio of 166.7.

The radial component of the axial velocity profile in the liquid film ahead of the leading Taylor bubble is represented by power law function (Equation 14), with exponent n=16 for L/D =16.7, n=8 for L/D =83.3 and n=6 for L/D =16.7. Despite a decrease in the exponent as L/D ratio increases, a fully parabolic profile is not achieved. This suggests that further studies on higher L/D ratios should be conducted.

REFERENCES

[1] Levy, S. (1999). *Two-phase flow in complex systems.* John Wiley & Sons.

[2] Brill, J. P. (2010). Modeling multiphase flow in pipes. *Society of Petroleum Engineers.* doi:10.2118/0210-016-TWA. 2: SPE-0210-016-TWA.

[3] Frooqnia, A. (2014). *Numerical simulation and interpretation of borehole fluid-production measurement* (PhD thesis). The University of Texas at Austin.

[4] Saffari, H., Moosavi, R., Nouri, N. M., & Lin, C. (2014). Prediction of hydrodynamic entrance length for single and two-phase flow in helical coils. *Chemical Engineering and Processing: Process Intensification,* 869-21.

[5] Morgado, A. O., Miranda, J. M., Araújo, J. D. P., & Campos, J. B. L. M. (2016). Review on vertical gas–liquid slug flow. *International Journal of Multiphase Flow,* 85348-368.

[6] Kaji, R., Azzopardi, B. J., & Lucas, D. (2009). Investigation of flow development of co-current gas–liquid vertical slug flow. *International Journal of Multiphase Flow*, 35(4), 335-348.

[7] Imada, F. H., Saltara, F., & Balino, J. F. (2013). Numerical study of the churn-slug transition dynamics in vertical upward air-water flows. In C. A. Brebbia & P. Vorobieff (Eds.), *Computational methods in multiphase flow VII* (VII ed., pp.101-114). Ashurst Lodge, UK: WIT Press.

[8] Abdulkadir, M., Hernandez-Perez, V., Abdulkareem, L., Lowndes, I. S., & Azzopardi, B. J. (2010). Characteristics of slug flow in a vertical riser. *Society of Petroleum Engineers*. doi:10.2118/140681-MS

[9] Zabaras, G. J. (2000). Prediction of slug frequency for gas/liquid flows. *Society of Petroleum Engineers,* J2: SPE-65093-PA.

[10] Abdulkadir, M., Hernandez-Perez, V., Lo, S., Lowndes, I. S., & Azzopardi, B. J. (2015). Comparison of experimental and Computational Fluid Dynamics (CFD) studies of slug flow in a vertical riser. *Experimental Thermal and Fluid Science, 68,* 468-483.

[11] Brennen, C. E. (2005). *Fundamentals of multiphase flow*. Cambridge University Press.

[12] Wan, R. G., Liu, Y., & Wang, J. (2007). A multiphase flow approach to modeling sand production using finite elements. *Petroleum Society of Canada*. doi:10.2118/07-04-04.

[13] Araújo, J. D. P., Miranda, J. M., & Campos, J. B. L. M. (2013). Simulation of slug flow systems under laminar regime: Hydrodynamics with individual and a pair of consecutive Taylor bubbles. *Journal of Petroleum Science and Engineering, 111,* 1-14.

[14] Mayor, T. S., Ferreira, V., Pinto, A. M. F. R., & Campos, J. B. L. M. (2008). Hydrodynamics of gas–liquid slug flow along vertical pipes in turbulent regime–An experimental study. *International Journal of Heat and Fluid Flow, 29*(4), 1039-1053.

[15] Morgado, A. O., Miranda, J. M., Araújo, J. D. P., & Campos, J. B. L. M. (2016). Review on vertical gas–liquid slug flow. *International Journal of Multiphase Flow, 85,* 348-368.

[16] Davies, R., & Taylor, G. (1950). The mechanics of large bubbles rising through extended liquids and through liquids in tubes. *Proceedings of the Royal Society of London A: Mathematical, Physical and Engineering Sciences,* 375-390.

[17] Griffith, P., & Wallis, G. B. (1961). Two-phase slug flow. *Journal of Heat Transfer, 83*(3), 307-318.

[18] Davidson, J., Nicklin, D., & Wilkes, J. (1962). Two Phase Flow in Vertical Tubes. *Trans.Inst. Chem. Engr,* 40-61.

[19] Brown, R. (1965). The mechanics of large gas bubbles in tubes: I. Bubble velocities in stagnant liquids. *The Canadian Journal of Chemical Engineering, 43*(5), 217-223.

[20] Collins, R., De Moraes, F., Davidson, J., & Harrison, D. (1978). The motion of a large gas bubble rising through liquid flowing in a tube. *Journal of Fluid Mechanics, 89*(03), 497-514.

[21] Xia, G., Cui, Z., Liu, Q., Zhou, F., & Hu, M. (2009). A model for liquid slug length distribution in vertical gas-liquid slug flow. *Journal of Hydrodynamics, Ser. B, 21*(4), 491-498.

[22] Wang, Y., Yan, C., Cao, X., Sun, L., Yan, C., & Tian, Q. (2014). Hydrodynamics of slug flow in a vertical narrow rectangular channel under laminar flow condition. *Annals of Nuclear Energy,* 73465-477.

[23]Santos, L. M. T., & Coelho Pinheiro, M. N. (2014). Flow around individual Taylor bubbles rising in a vertical column with water: Effect of gas expansion. *International Journal of Multiphase Flow,* 6339-6351.

[24]Mayor, T. S., Pinto, A. M. F. R., & Campos, J. B. L. M. (2008). On the gas expansion and gas hold-up in vertical slugging columns—A simulation study. *Chemical Engineering and Processing: Process Intensification, 47*(5), 799-815.

[25]Kaji, R., & Azzopardi, B. J. (2010). The effect of pipe diameter on the structure of gas/liquid flow in vertical pipes. *International Journal of Multiphase Flow, 36*(4), 303-313.

[26]Taitel, Y., Bornea, D., & Dukler, A. (1980). Modelling flow pattern transitions for steady upward gas–liquid flow in vertical tubes. *AIChE Journal, 26*(3), 345-354.

[27]Sharaf, S., van der Meulen, G.P., Agunlejika, E. O., & Azzopardi, B. J. (2016). Structures in gas–liquid churn flow in a large diameter vertical pipe. *International Journal of Multiphase Flow, 78,* 88-103.

[28]Rosa, E. S., & Souza, M. A. S. F. (2015). Spatial void fraction measurement in an upward gas–liquid flow on the slug regime. *Flow Measurement and Instrumentation, 46,* 139-154.

[29]Mayor, T. S., Pinto, A. M. F. R., & Campos, J. B. L. M. (2007). Hydrodynamics of gas–liquid slug flow along vertical pipes in turbulent regime: A simulation study. *Chemical Engineering Research and Design, 85*(11), 1497-1513.

[30]Akanji, L., & Matthai, S. (2010). Finite element-based characterization of pore-scale geometry and its impact on fluid flow. *Transport in Porous Media, 81*(2), 241-259.

[31]Fluent, A. (2006). *Fluent 6.3 documentation*. Lebanon, NH: Fluent Inc.

[32]Launder, B. E., & Spalding, D. B. (1974). The numerical computation of turbulent flows. *Computer Methods in Applied Mechanics and Engineering, 3*(2).

[33]Yakhot, V., & Orszag, S. A. (1986). Renormalization group analysis of turbulence.i. basici theory. *Journal of Scientific Computer, 1*(1), 1-35

[34]Hirt, C. W., & Nichols, B. D. (1981). Volume of fluid (vof) mehtod for dynamics of free surfaces. *Journal of Computational Physics, 39,* 201-225.

[35]Brackbill, J. U., Kothe, D. B., & Zemach, C. (1992). A continuum method for modellling surface tension. *Journal of Computational Physics, 100,* 335-354.

[36]Zheng, D., He, X., & Che, D. (2007). CFD simulations of hydrodynamic characteristics in a gas–liquid vertical upward slug flow. *International Journal of Heat and Mass Transfer, 50*(21), 4151-4165.

[37]Da Riva, E., & Del Col, D. (2009). Numerical simulation of churn flow in a vertical pipe. *Chemical Engineering Science, 64*(17), 3753-3765.

[38]Versteeg, H. K., & Malalasekera, W. (2007). *An introduction to computational fluid dynamics: The finite volume method.* Pearson Education.

[39]Patankar, S. V., & Spalding, D. B. (1972). A calculation procedure for heat, mass and momentum transfer in three-dimensional parabolic flows. *International Journal of Heat and Mass Transfer, 15*(10), 1787-1806.

[40]Polonsky, S., Shemer, L., & Barnea, D. (1999). The relation between the Taylor bubble motion and the velocity field ahead of it. *International Journal of Multiphase Flow, 25*(6-7), 957-975.

[41]Shao, N., Salman, W., Gavriilidis, A., & Angeli, P. (2008). CFD simulations of the effect of inlet conditions on Taylor flow formation. *International Journal of Heat and Fluid Flow, 29* (6), 1603-1611.

[42]Shen, X., Matsui, R., Mishima, K., & Nakamura, H. (2010). Distribution parameter and drift velocity for two-phase flow in a large diameter pipe. *Nuclear Engineering and Design, 240*(12), 3991-4000.

[43]Liu, H., Vandu, C. O., & Krishna, R. (2005). Hydrodynamics of Taylor flow in vertical capillaries: Flow regimes, bubble rise velocity, liquid slug length, and pressure drop. *Industrial & Engineering Chemistry Research, 44*(14), 4884-4897.

[44]Ansari, M. R., & Azadi, R. (2016). Effect of diameter and axial location on upward gas–liquid two-phase flow patterns in intermediate-scale vertical tubes. *Annals of Nuclear Energy, 94,* 530-540.

[45]Johansen, S. T., Mo, S., Meese, E., Oliveira, J. E. S., Reyes, J. F. R., & Carneiro, J. N. E. (2015). *CFD simulations of multiphase flows containing large scale interfaces and dispersed phases with selected production technology applications.* Offshore Technology Conference. doi:10.4043/26303-MS

[46]Szalinski, L., Abdulkareem, L. A., Da Silva, M. J., Thiele, S., Beyer, M., Lucas, D.,…Azzopardi, B. J. (2010). Comparative study of gas–oil and gas–water two-phase flow in a vertical pipe. *Chemical Engineering Science, 65*(12), 3836-3848.

[47]Sasaki, S., Hayashi, K., & Tomiyama, A. (2016). Effects of liquid height on gas holdup in air–water bubble column. *Experimental Thermal and Fluid Science, 72,* 67-74.

[48]Wang, Y., Yan, C., Sun, L., & Yan, C. (2014). Characteristics of slug flow in a vertical narrow rectangular channel. *Experimental Thermal and Fluid Science, 53,* 1-16.

[49]Icardi, M., Ronco, G., Marchisio, D. L., & Labois, M. (2014). Efficient simulation of gas–liquid pipe flows using a generalized population balance equation coupled with the algebraic slip model. *Applied Mathematical Modelling, 38*(17-18), 4277-4290.

